Carbon Quantum Dots Embedded Graphitic Carbon Nitride for Fluorescent Imaging-guided Combined Tumor Therapy

Xingyu Wang,[†a,b] Jiahui Zhang,[†c,b] Chengyang Fang,[a,b] Xinyi Shi,[a,b] Jiaping Zhao,[a,b] Wenchu Lin,[*d] Hui Wang[*a,b] and Rongrong Nie,[*e]

[a.] *University of Science and Technology of China, Hefei 230026, Anhui, P. R. China.*

[b.] *High Magnetic Field Laboratory, Hefei Institutes of Physical Science, Chinese Academy of Sciences, Hefei 230031, Anhui, P. R. China.*

[c.] *Department of Blood Transfusion, The First Affiliated Hospital of USTC, University of Science and Technology of China. Hefei, Anhui, 230001.China.*

[d.] *The Second Affiliated Hospital, School of Medicine, The Chinese University of Hong Kong, Shenzhen & Longgang District People's Hospital of Shenzhen, Shenzhen 518172, Guangdong, P. R. China.*

[e.] *Nanjing Stomatological Hospital Medical School of Nanjing University, Nanjing 210008, Jiangsu, P. R. China*

† These authors contributed equally to this work.

**Corresponding author: hw39@hmfl.ac.cn (H. Wang), nrr63@nju.edu.cn (R. Nie), linwenchu@ustc.edu.cn (W. Lin)*

Table S1: Comparison of PCE among various carbon-based photothermal agents

Photothermal reagent	Wavelength	PCE	references
plys-CDs	655 nm	54.9%	[1]
PBPTV@mPEG	808 nm	38.1%	[2]
FeNC@PEG	808 nm	34%	[3]
DCNPs@C@PEI@FA	808 nm	30%	[4]
Fe_3O_4@C@Pt-Ce6	808 nm	28.28%	[5]
Fe_{50}-Zn-NC_{900}	808 nm	81.3%	[6]
yCDs-Ce6	808 nm	54.2%	[7]
SNB	808 nm	33.1%	[8]
GCN-CQD	808 nm	67.08%	This work
BC-PDA-Hb	1064 nm	47.8%	[9]
SPNE	1064 nm	88.8%	[10]
$SSPN_{iNO}$	1064 nm	57.4%	[11]
CSMN2	1064 nm	31.6%	[12]
GQDs	1064 nm	33.45%	[13]
FDCN	1064 nm	36.3%	[14]

Supplementary Figures

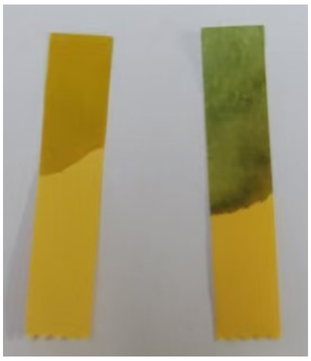

Figure S1. Wet pH test strip (left) and wet test strip placed on the reaction solution when the autoclave was opened at the end of reaction (right). Alkaline NH_3 could turn the pH test strip green, indicating that NH_3 was generated during the synthesis of GCN-CQD.

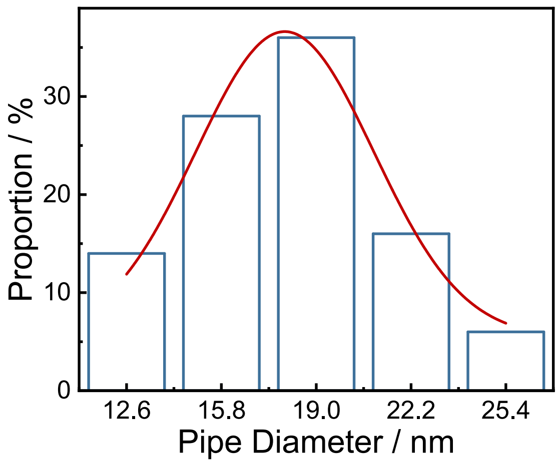

Figure S2. Size distribution of carbon nanofiber diameter.

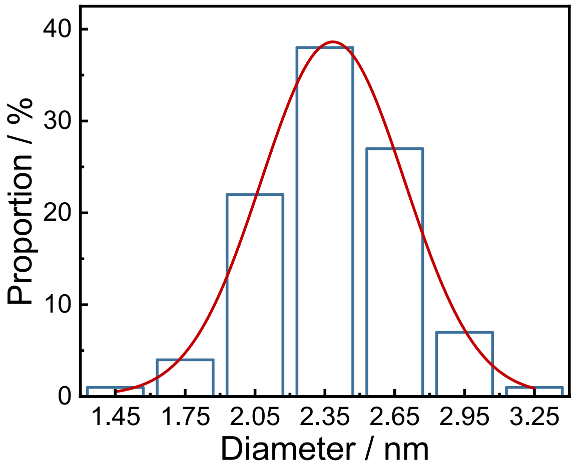

Figure S3. Size distribution of the carbon quantum dots.

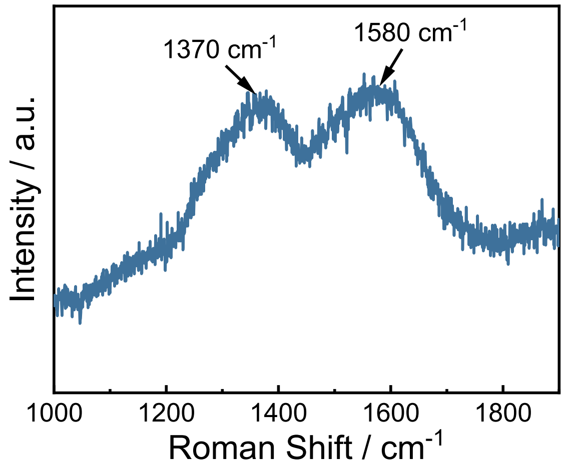

Figure S4. Raman spectrum of the GCN-CQD.

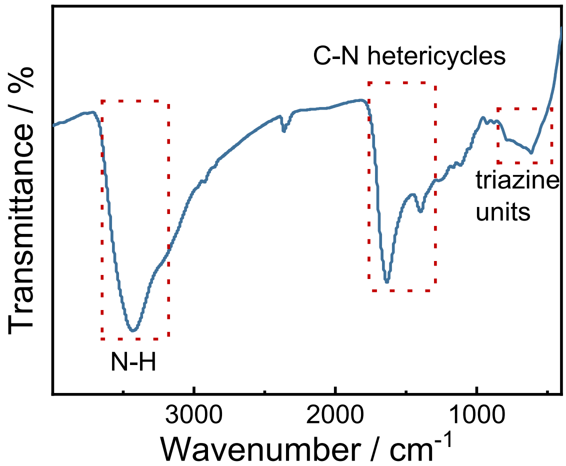

Figure S5. FT-IR spectrum of the GCN-CQD.

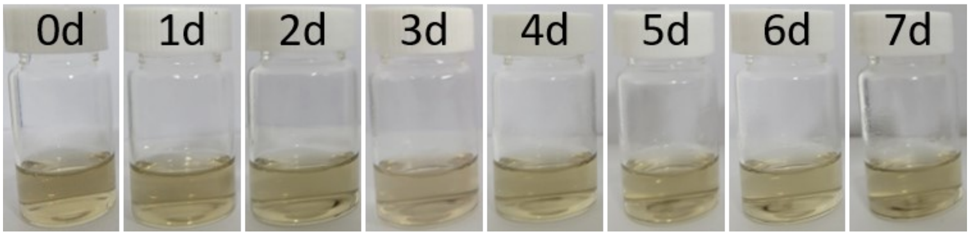

Figure S6. Optical pictures of the as-synthesized GCN-CQD dispersed in water for over 7 days. Results shown that the GCN-CQD possess excellent aqueous dispersibility.

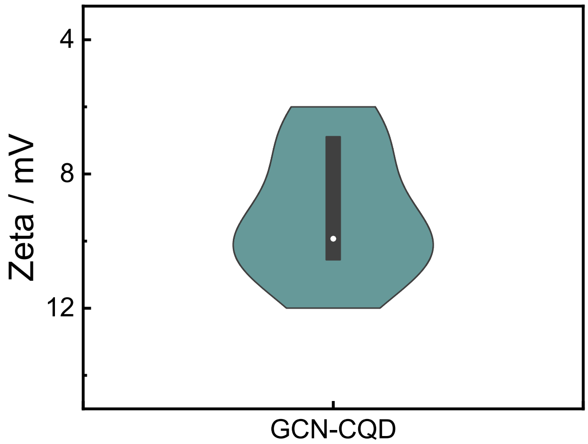

Figure S7. Zeta potential of the GCN-CQD.

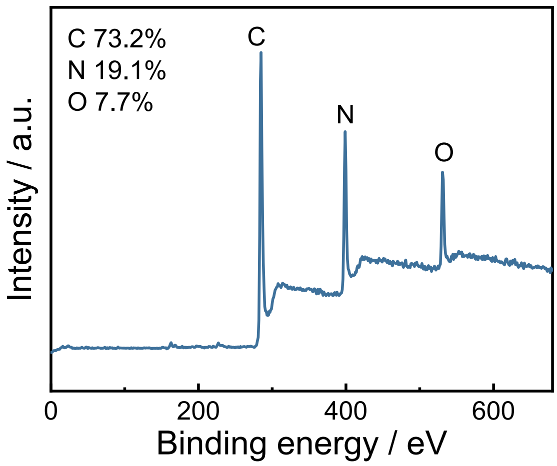

Figure S8. XPS scanning spectrum of the GCN-CQD.

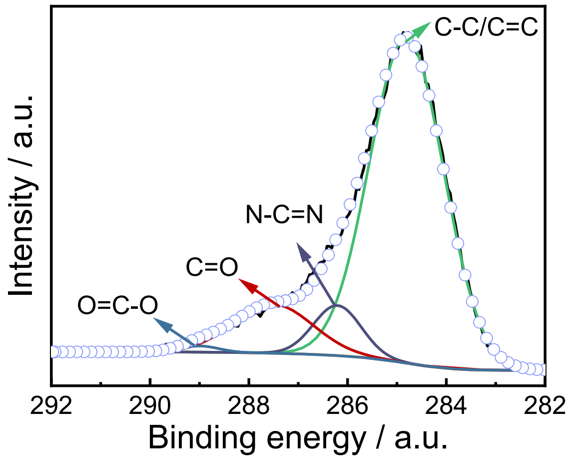

Figure S9. XPS high-resolution survey scans of C 1s in the GCN-CQD.

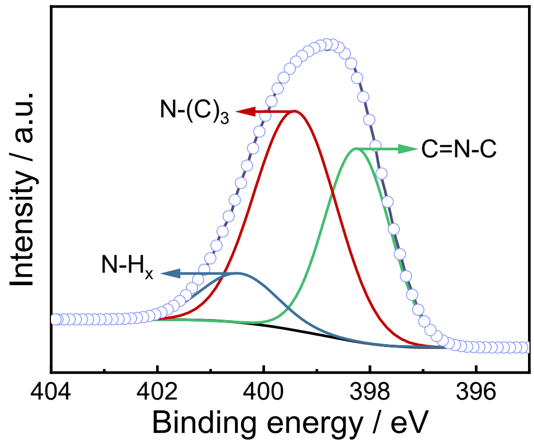

Figure S10. XPS high-resolution survey scans of N 1s in the GCN-CQD.

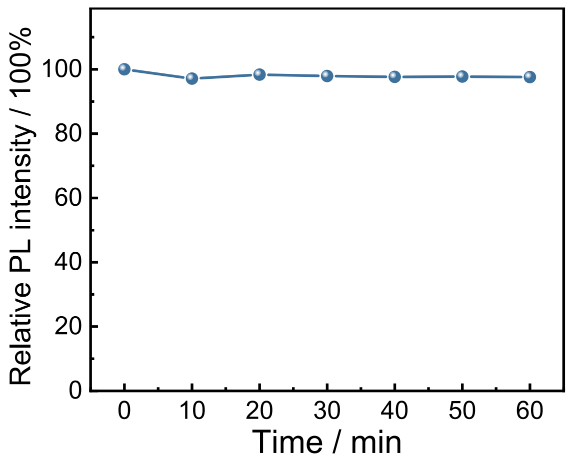

Figure S11. Relative fluorescence change of GCN-CQD irradiated at 334 nm for 60 min.

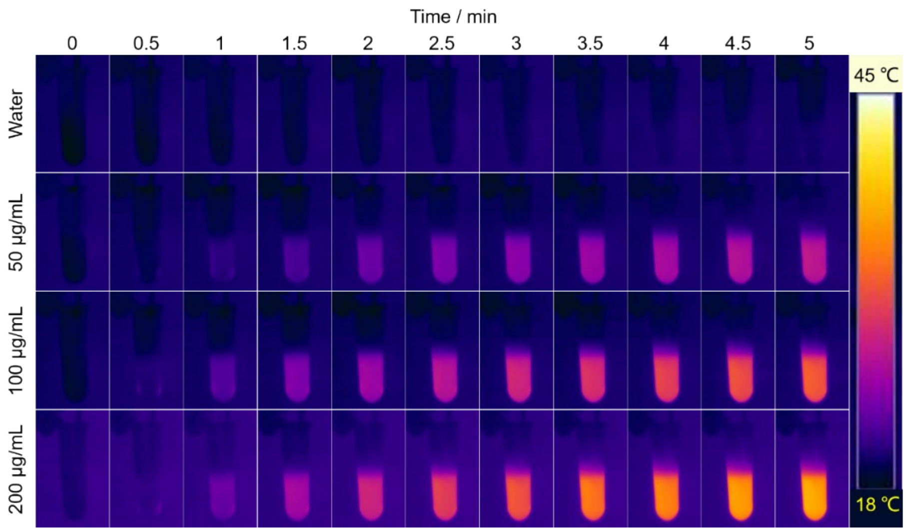

Figure S12. IR thermal images of different concentrations of GCN-CQD solution under 808 nm irradiation for 5 min

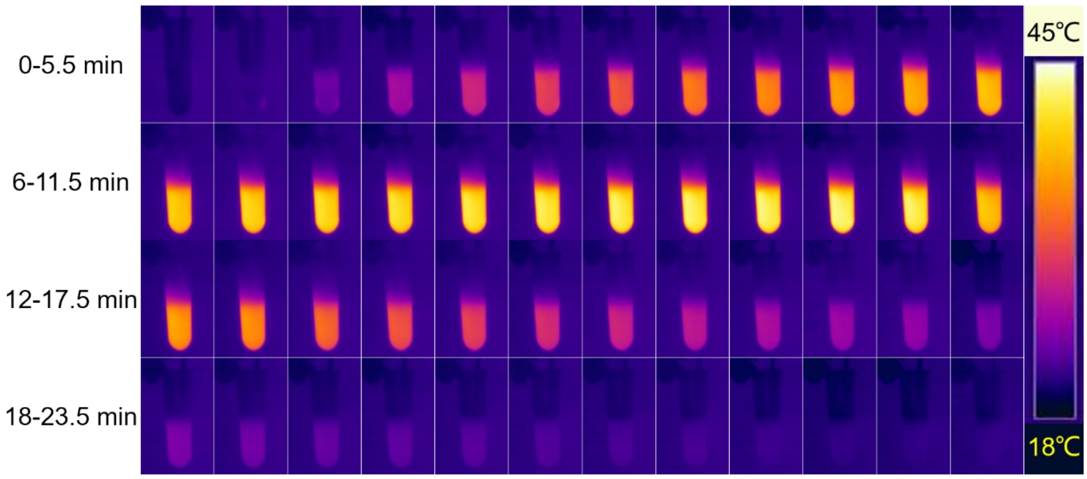

Figure S13. IR thermal images of GCN-CQD solution (200 μg mL^{-1}) irradiated with 808 nm laser to saturation temperature.

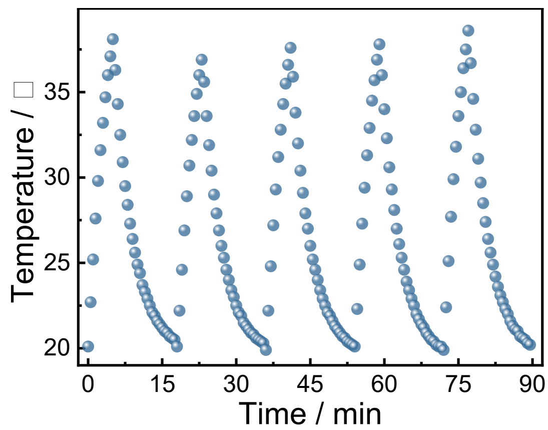

Figure S14. The GCN-CQD's heating curves after five cycles of dispersion in distilled water.

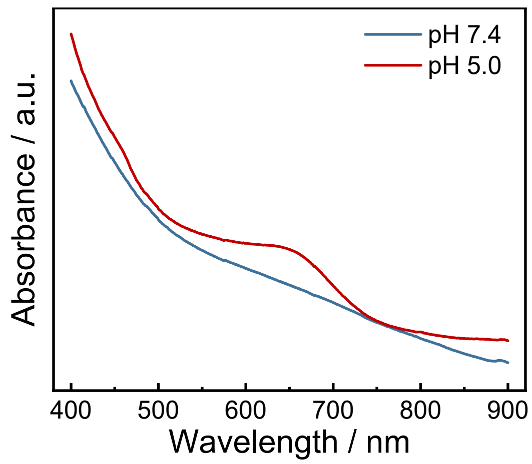

Figure S15. The UV-Vis-NIR spectra of the mixed neutral solution (pH 7.4) and acid solution (pH 5.0) containing TMB, H_2O_2, and GCN-CQD. The absorption peak generated by TMB capturing ·OH is at 651 nm, which indicates that GCN-CQD in acidic conditions can generate more ·OH.

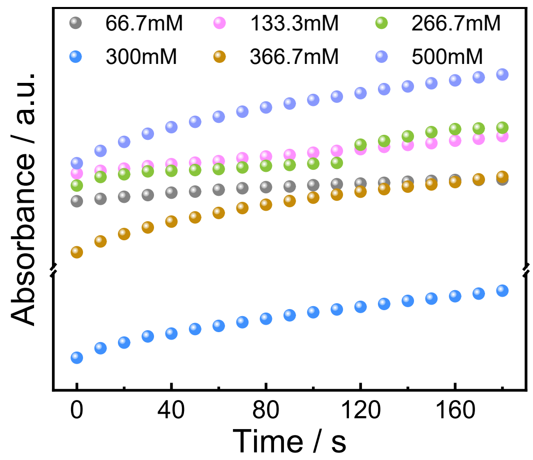

Figure S16. Detailed test data on the Michaelis-Menten fitting curves of the GCN-CQD.

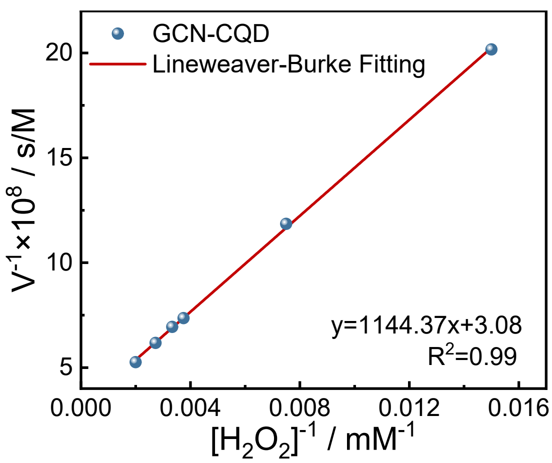

Figure S17. The Lineweaver-Burke fitting (double reciprocal) of Michaelis-Menten fitting curve of the GCN-CQD under 150 μL TMB (10 $mg \cdot mL^{-1}$).

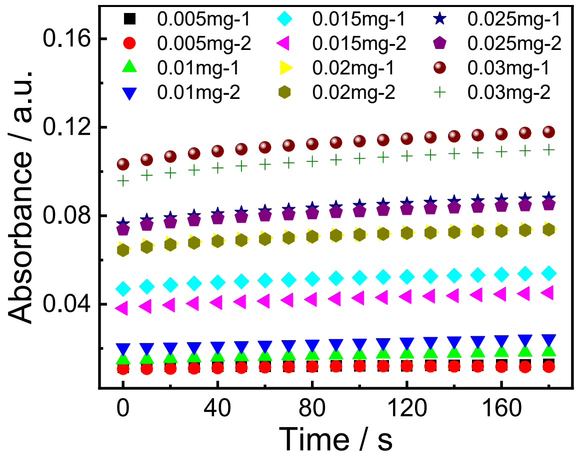

Figure S18. Detailed test data on the SA of the GCN-CQD.

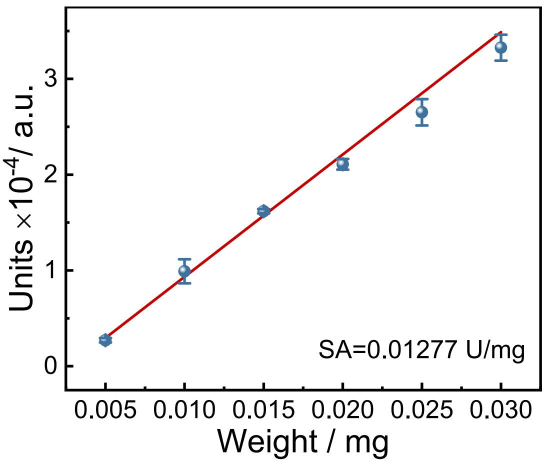

Figure S19. SA of the as-synthesized GCN-CQD.

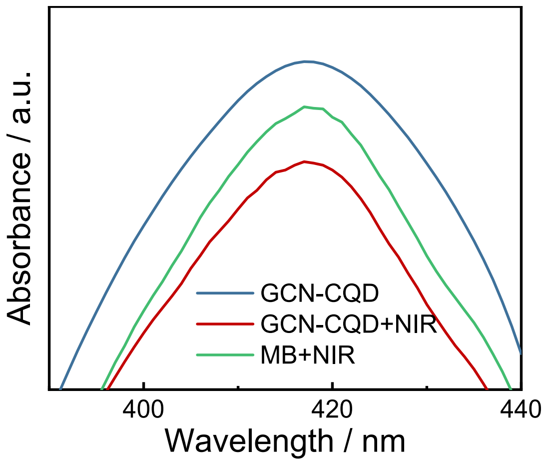

Figure S20. UV-Vis spectra of the mixed solution after 30 minutes of reaction in different reaction systems (GCN-CQD/DPBF, GCN CQD/DPBF+NIR, and MB/DPBF+NIR).

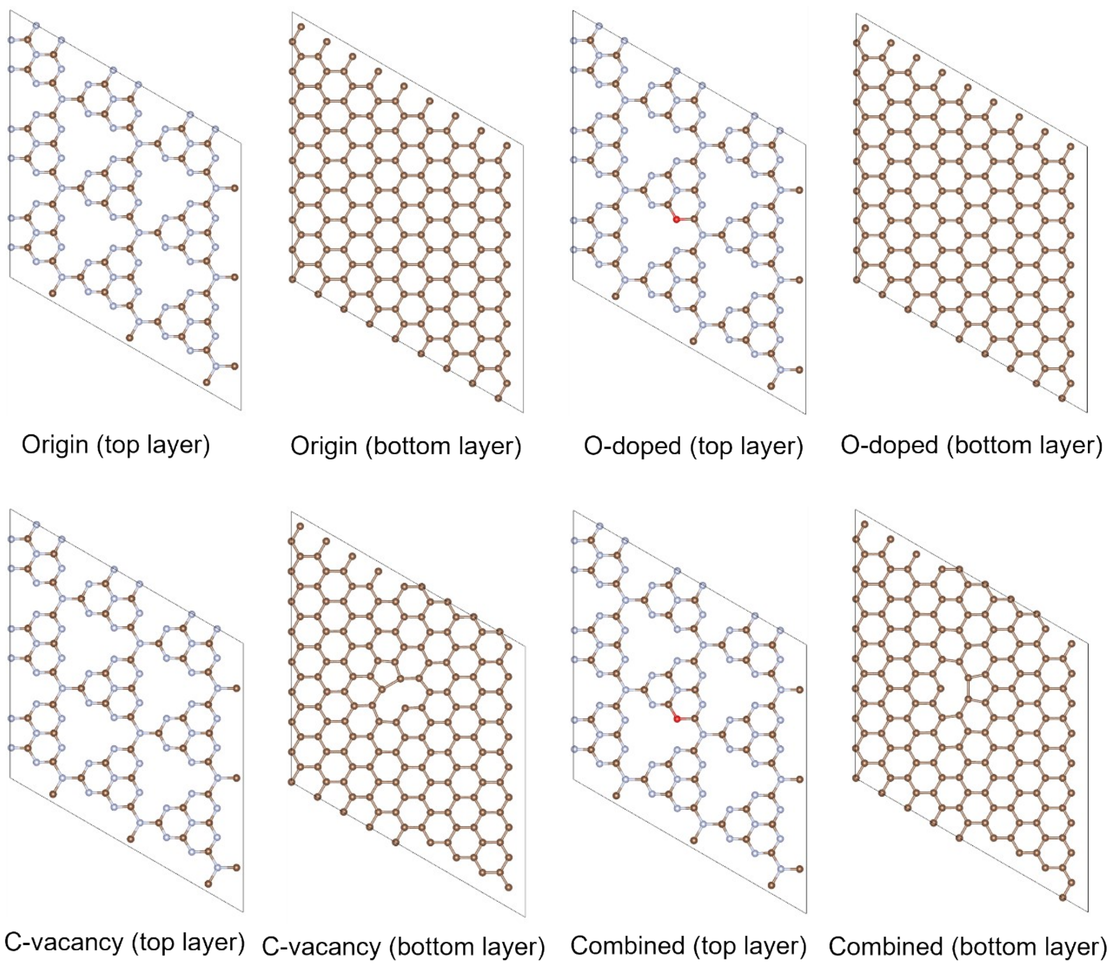

Figure S21. Top view of four simulated models.

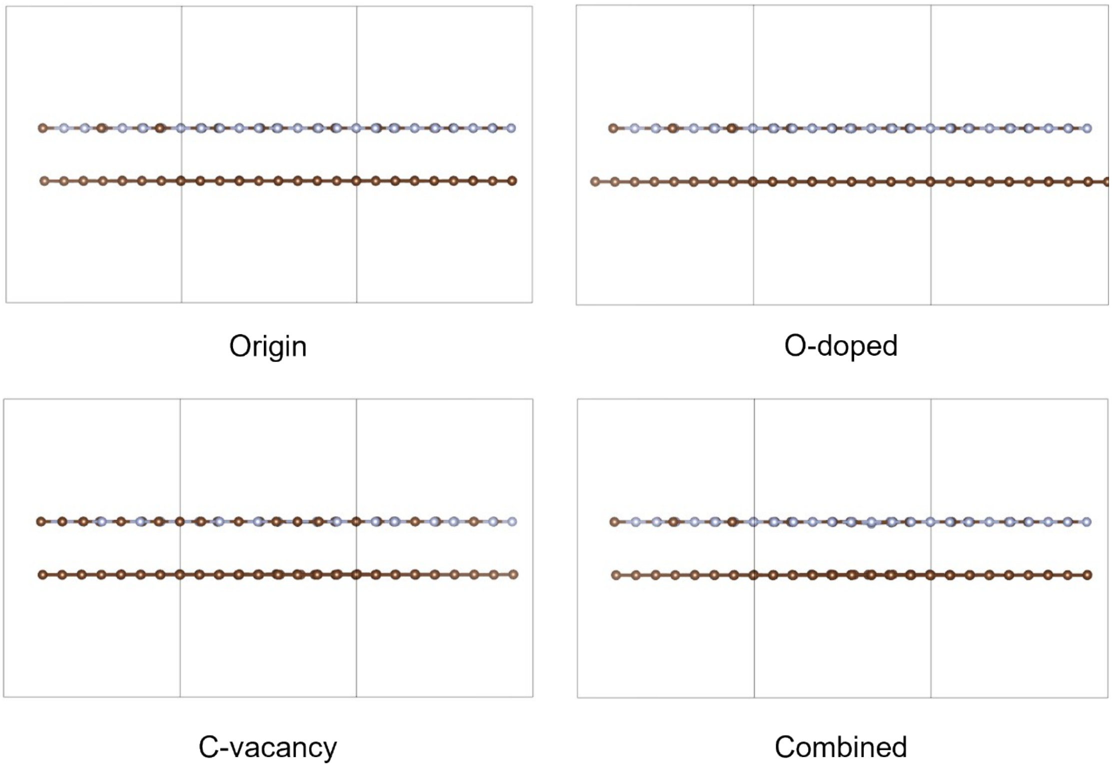

Figure S22. Side view of four simulated models.

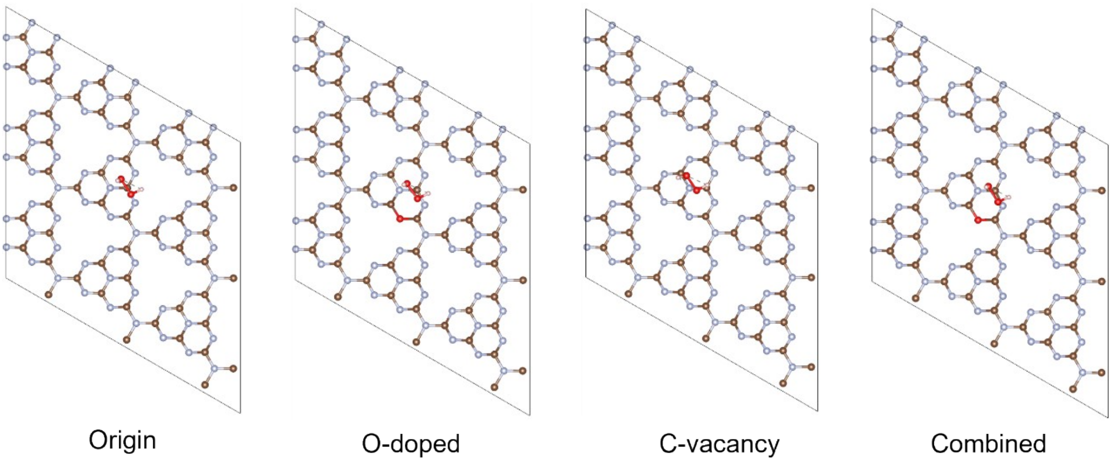

Figure S23. Top view of four simulated models absorbed with H_2O_2. Bottom layer is omitted for clarity.

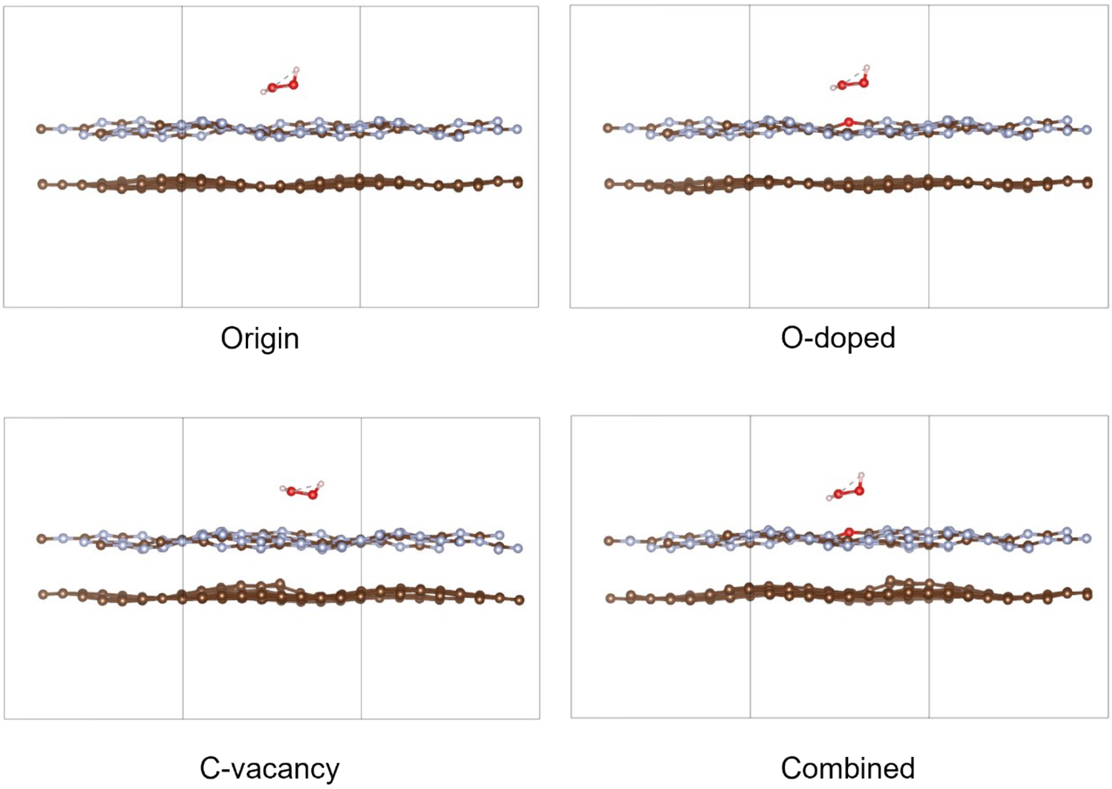

Figure S24. Side view of four simulated models absorbed with H_2O_2.

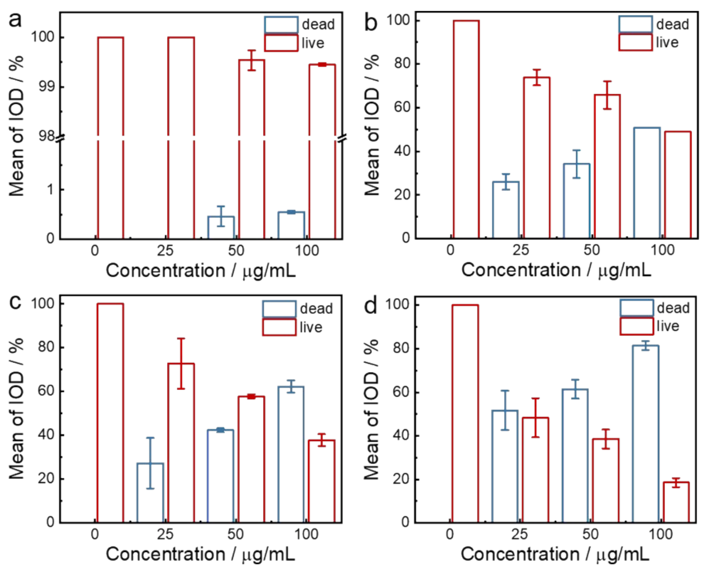

Figure S25. Quantified the confocal fluorescence intensity of calcein-AM/PI double-stained 4T1 cells treated with GCN-CQD of under different conditions (a: pH 7.4, b: pH7.4+NIR, c: pH 5.0, d: pH 5.0+NIR). The statistics showed that cell survival rate was inversely proportional to concentration, acidity, and laser irradiation time under different conditions.

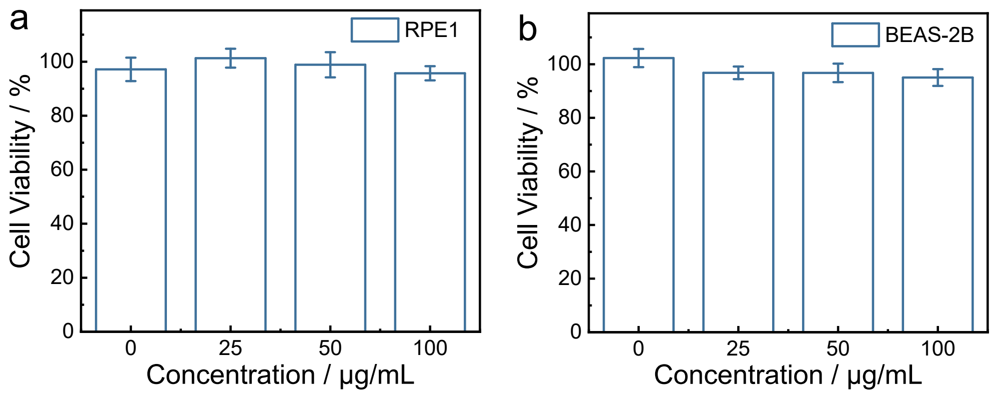

Figure S26. The viability of hTERT (a) RPE-1, (b) BEAS-2B cells after being treated with the GCN-CQD.

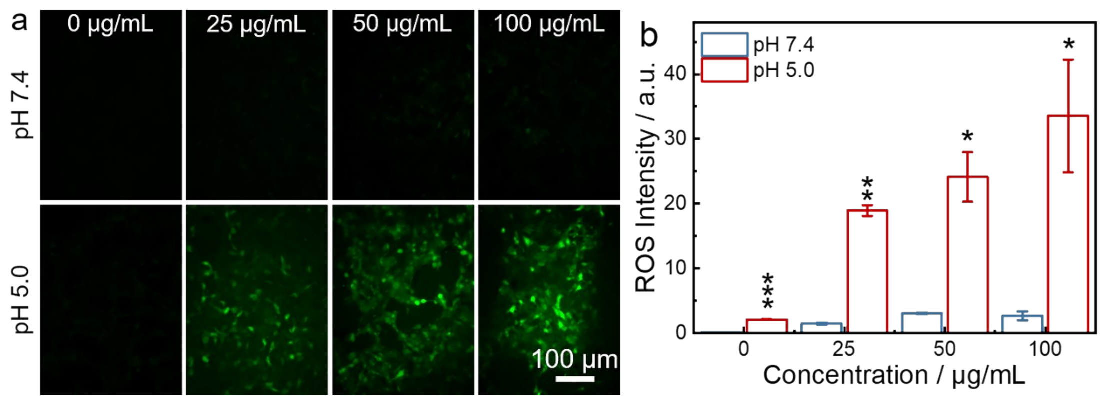

Figure S27. (a) Confocal images, (b) ROS intensity of DCFH-DA-stained 4T1 cells treated with the GCN-CQD at pH 7.4 or 5.0.

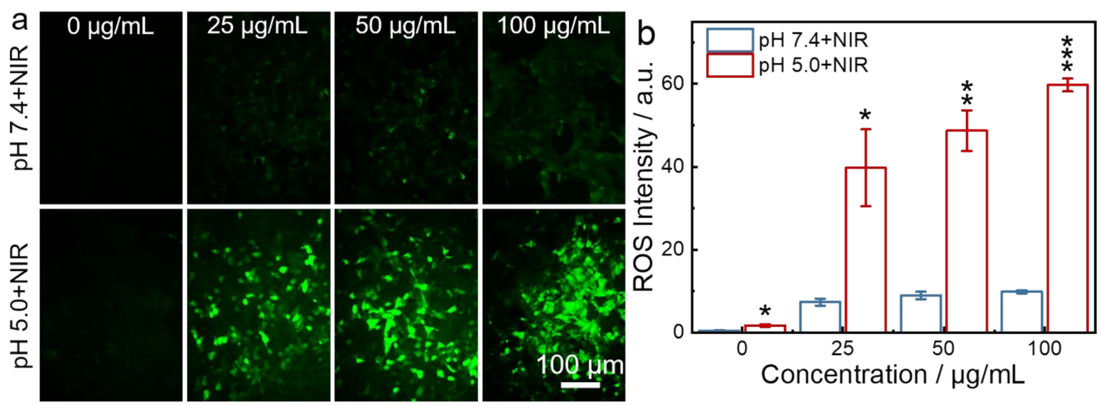

Figure S28. (a) Confocal images, (b) ROS intensity of DCFH-DA-stained 4T1 cells treated with the GCN-CQD at pH 7.4+NIR or pH 5.0+NIR.

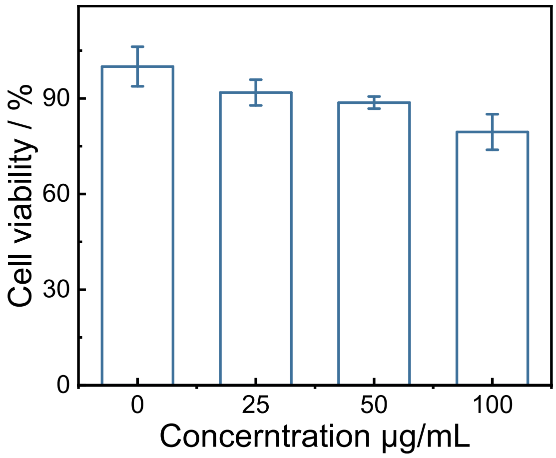

Figure S29. Cell survival rate under intermittent laser irradiation (1 minute on/1 minute off).

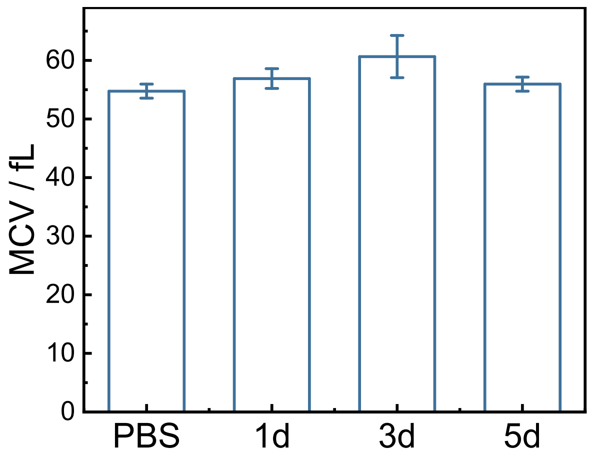

Figure S30. MCV data of untreated mice (control) and mice treated with GCN-CQD after 1 d, 3 d, and 5 d (n=3).

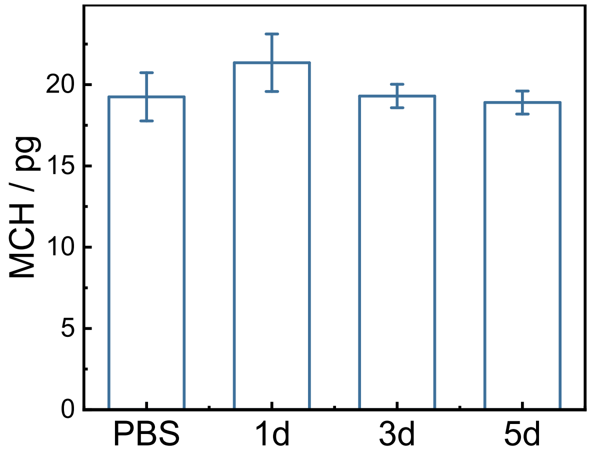

Figure S31. MCH data of untreated mice (control) and mice treated with GCN-CQD after 1 d, 3 d, and 5 d (n=3).

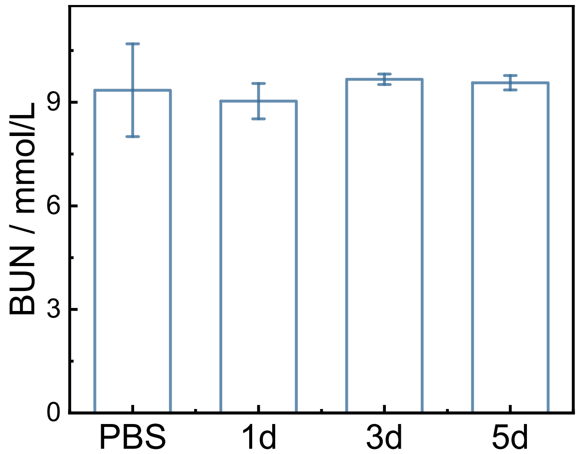

Figure S32. BUN data of untreated mice (control) and mice treated with GCN-CQD after 1 d, 3 d, and 5 d (n=3).

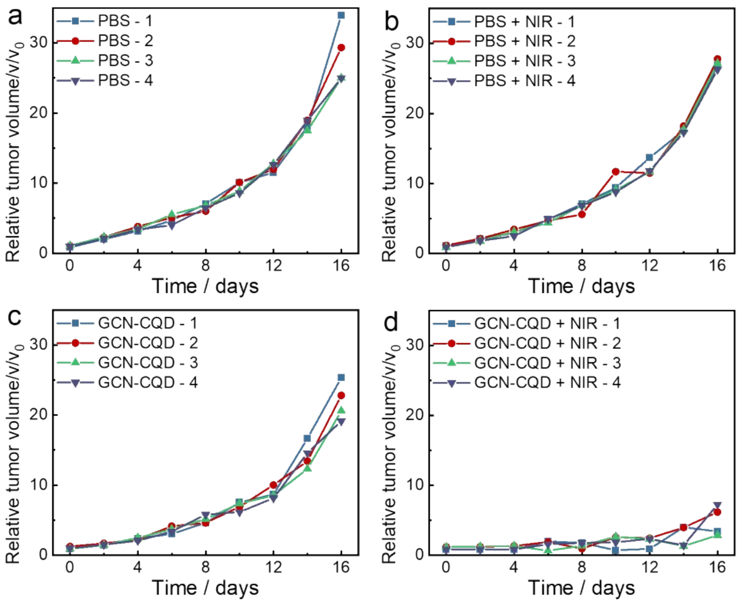

Figure S33. Tumor growth curves of mice treated by PBS and the GCN-CQD over 16 days. (a) PBS, (b) PBS + NIR, (c) GCN-CQD, (d) GCN-CQD + NIR.

References:

1. Z. Li, H. Cheng, B. Wang, L. Wang, J. Wu, B. Zhang, Z. Tang and S. Qu, Polylysine-modified near-infrared-emitting carbon dots assemblies: Amplification of tumor accumulation for enhanced tumor photothermal therapy, *J. Colloid Interface Sci.*, 2024, **668**, 132-141.
2. G. Ma, Z. Liu, C. Zhu, H. Chen, R. T. K. Kwok, P. Zhang, B. Z. Tang, L. Cai and P. Gong, H_2O_2-Responsive NIR-II AIE Nanobomb for Carbon Monoxide Boosting Low-Temperature Photothermal Therapy, *Angew. Chem., Int. Ed.*, 2022, **61**, e202207213.
3. D. Li, M. Zhang, Y. Huang, X. Hu and J. Hu, FeNC with atomically dispersed iron atoms as a photosensitizer for combined photodynamic and photothermal therapy, *Flatchem*, 2024, **45**, 100663.
4. S. Peng, L. Wang, L. Liu, L. Song, J. Shi, H. Zheng, J. Xu, R. Rong and Y. Zhang, Inhibition of Pro-Survival Autophagy Induced by Rare-Earth Nanocomposites for Promoting Photothermal Therapy of Visualized Tumors, *Adv. Healthcare Mater.*, 2023, **12**, 2202117.
5. Z. Xu, J. Chen, Y. Li, T. Hu, L. Fan, J. Xi, J. Han and R. Guo, Yolk-shell Fe_3O_4@Carbon@Platinum-Chlorin e6 nanozyme for MRI-assisted synergistic catalytic-photodynamic-photothermal tumor therapy, *J. Colloid Interface Sci.*, 2022, **628**, 1033-1043.
6. W. Fu, Q. Lu, S. Xing, L. Yan and X. Zhang, Iron-Doped Metal-Zinc-Centered Organic Framework Mesoporous Carbon Derivatives for Single-Wavelength NIR-Activated Photothermal/Photodynamic Synergistic Therapy, *Langmuir*, 2023, **39**, 6505-6513.
7. C. Yan, C. Wang, X. Shao, Y. Teng, P. Chen, X. Hu, P. Guan and H. Wu, Multifunctional Carbon-Dot-Photosensitizer Nanoassemblies for Inhibiting Amyloid Aggregates, Suppressing Microbial Infection, and Overcoming the Blood-Brain Barrier, *ACS Appl. Mater. Interfaces*, 2022, **14**, 47432–47444.
8. G. Ma, Q. Ding, Y. Wang, Z. Zhang, Y. Zhang, H. Shi, L. Cai, P. Gong, P. Zhang, Z. Cheng and J. S. Kim, Precision Photothermal Therapy at Mild Temperature: NIR-II Imaging-Guided, H_2O_2-Responsive Stealth Nanobomb, *Adv. Healthcare Mater.*, 2024, 2402767.
9. C. Chen, W. Zhang, Y. Ouyang, Y. Tan, S. Zhao, Y. Chen, L. He, S.-Y. Lu, H. Ran and H. Liu, Hemoglobin-Decorated Boron-Carbon Nanosheets with Catalytic Ability and Near-Infrared II Light Response for Tumor Photothermal-Chemodynamic Therapy, *ACS Appl. Nano Mater.*, 2023, **6**, 7572-7581.
10. C. Xu, Y. Jiang, Y. Han, K. Pu and R. Zhang, A Polymer Multicellular Nanoengager for Synergistic NIR-II Photothermal Immunotherapy, *Adv. Mater.*, 2021, **33**, 2008061.
11. J. Liu, D. Cheng, A. Zhu, M. Ding, N. Yu and J. Li, Neutrophil-Targeting Semiconducting Polymer Nanotheranostics for NIR-II Fluorescence Imaging-Guided Photothermal-NO-Immunotherapy of Orthotopic Glioblastoma, *Adv. Sci.*, 2024, **11**, 2406750.
12. W. Shao, Q. Wei, S. Wang, F. Li, J. Wu, J. Ren, F. Cao, H. Liao, J.-Q. Gao, M. Zhou and D. Ling, Molecular engineering of D-A-D conjugated small molecule nanoparticles for high performance NIR-II photothermal therapy, *Mater. Horiz.*, 2020, **7**, 1379-1386.
13. H. Liu, C. Li, Y. Qian, L. Hu, J. Fang, W. Tong, R. Nie, Q. Chen and H. Wang, Magnetic-induced graphene quantum dots for imaging-guided photothermal therapy in the second near-infrared window, *Biomaterials*, 2020, **232**, 119700.
14. X. Wang, T. Song, X. Wu, Y. Lin, X. Shi, J. Qian, R. Nie and H. Wang, NIR-II Responsive Fe-Doped Carbon Nanoparticles for Photothermal-Enhanced Chemodynamic Synergistic Oncotherapy, *ACS Appl. Mater. Interfaces*, 2024, **16**, 46079-46089.